**Mechanics of Adhesives under Annular Confinement: Internal Pressure, Force, and Interfacial Area**

**Supporting Information**

*Hares Wahdat,[a] Paul Elzière,[b] Nicky Chan,[b] Alfred J. Crosby[a,*]*

*[a]: Polymer Science and Engineering Department, University of Massachusetts Amherst, Amherst, 01003 MA, USA*

*[b]: Saint-Gobain Research North America, 9 Goddard Road, Northborough, 01532 MA, USA*

**Corresponding author: acrosby@umass.edu*

# 1 Details about Preparation of PDMS Samples

Poly(dimethylsiloxane) (PDMS) samples with variable degree of cross-linking were prepared from a Sylgard™ 184 kit (Dow) consisting of base and cross-linker. Formulations with variable weigth ratios of base:cross-linker ratio (x:y) were prepared. After three degassing cycles, the formulations were poured into 2 mm- or 0.5 mm-thick 3D-printed molds glued on microscope slides. Curing of the formulations occurred for 20 h at 70 °C.

# 2 Details about Load Cell Used in Contact Adhesion Testing Instrument

The force, $F$, in the contact adhesion testing instrument was measured by a custom-built cantilever-based load cell which is sketched in S-Figure 1. The probe is attached to a rectangular aluminum sheet which serves as the cantilever. The cantilever is connected to an actuator (Burleigh Inchworm, Exfo) that controls the displacement. The force-measurement is achieved by fixing a capacitance sensor (PI D-510 021, Physik Instrumente, Germany) that connected to a signal conditioner (PI E-852, Physik Instrumente, Germany) above the cantilever. The capacitance sensor measures the deflection, $d$, of the cantilever, which is proportional to the force. Upon determination of a linear calibration curve as achieved by placing exact weights on the cantilever and determining the deflection while the probe is not in contact with any material, the force can be calculated from the deflection.

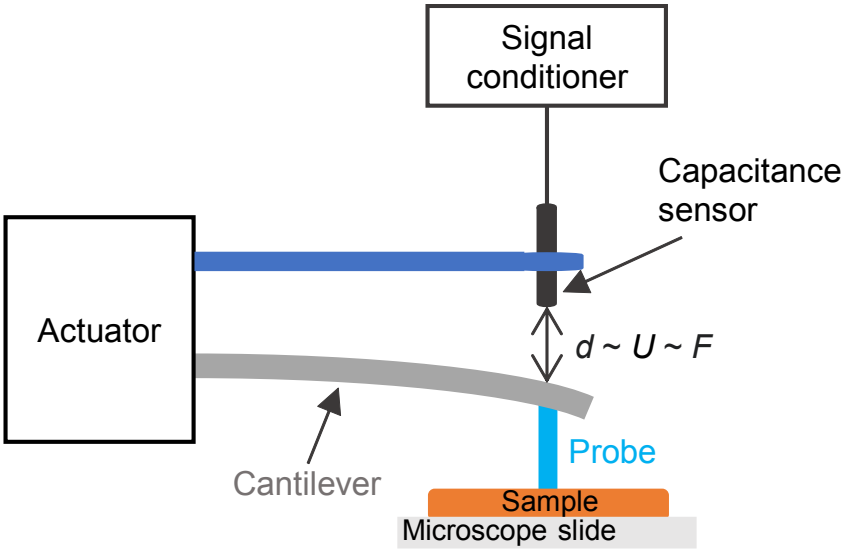


**S-Figure 1: Sketch of the load cell in the contact adhesion testing instrument. Both the aluminum cantilever and the capacitance sensor are attached to the actuator. The capacitance sensor measures a voltage difference between its bottom surface and the top surface of the cantilever. The voltage is proportional to the deflection, *d*, from which the force, *F*, can be calculated using a calibration curve.**

The true probe displacements, δ, were calculated from the raw displacement values measured by the actuator, δ', by accounting for the bending of the cantilever following $\delta = \delta' - K F$. $F$ is the contact force, and $K$ is the stiffness of the cantilever as determined from the slope of a force–displacement curve between the probe and a microscope slide.

# 3 Finite Element Analysis

## 3.1 *Details about the FEA Model*

All finite element analysis (FEA) simulations were conducted using a commercial version of ABAQUS/CAE 2018 (Dassault Systems). A three-dimensional model was used in all cases. Force-displacement relationships for axisymmetric contact between a rigid, annular probe and an elastic sample was simulated. The sample was an incompressible elastic material. Unless stated otherwise, $E$ was always $10^5$ Pa and $\nu$ was 0.4999. For the probe, $E$ was 2 GPa and $\nu$ was 0.3. The thickness, $h$, of the sample was varied. The outer radius, $a$, of the sample was kept constant, and the inner radius, $b$, was varied. The width and the length of the sample, $L$, were identical, and usually 10 times the sample's thickness. In all cases, the maximum probe displacements simulated were 0.01–0.1 μm, depending on the thickness to ensure a linear force–displacement relationship.

To simulate contact, a surface-to-surface contact with finite sliding between the interfacial nodes

of the sample and the probe was defined. Regarding interaction properties, the tangential behavior was

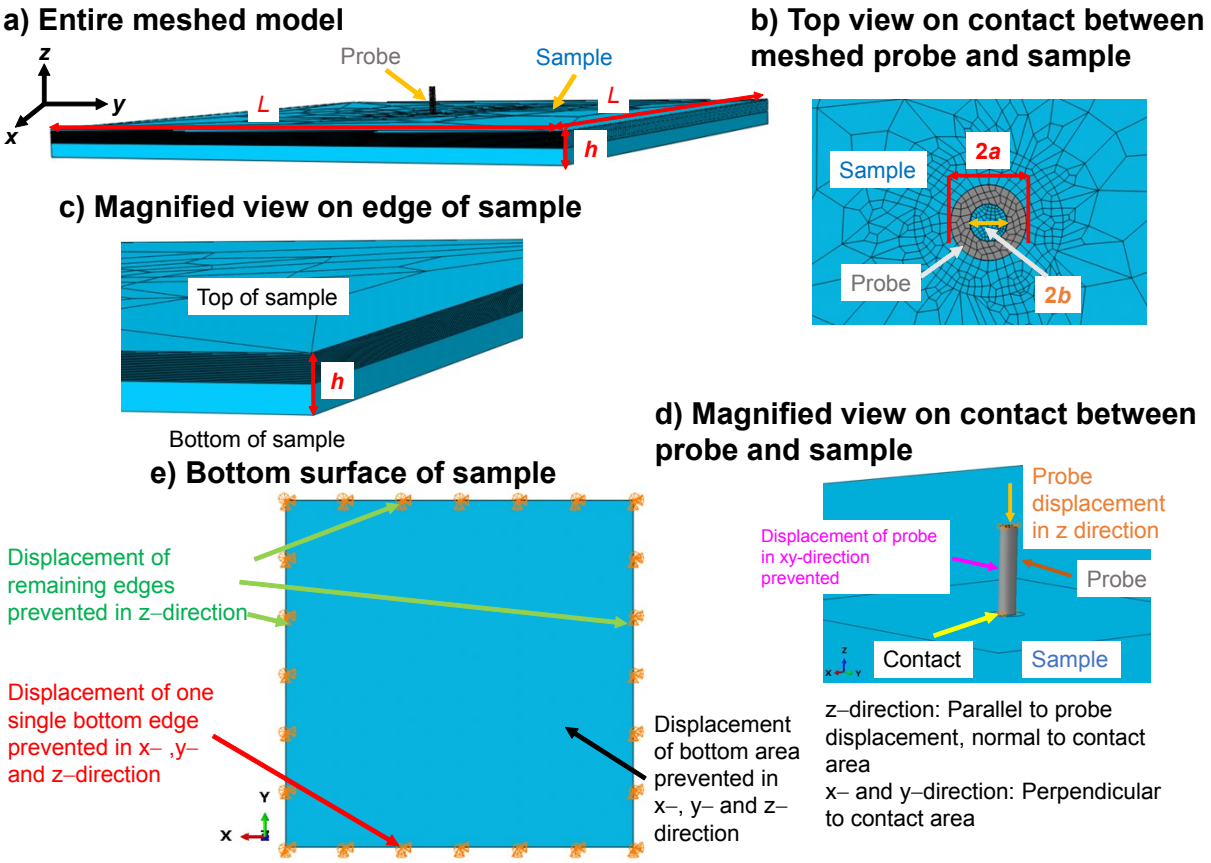


**S-Figure 2: Sketch of three-dimensional FEA model. The z-direction is parallel to the probe displacement and normal to the contact area, and both the x– and y-direction are perpendicular to the probe displacement, which is parallel to the z–direction. a) Side-view on entire meshed model. b) Top view on contact region between the probe and the sample. The mesh was finer at the contact region. For different values of *b*/*a*, the meshes of the probe and the sample were refined accordingly. c) Magnified view on edge of sample. From top to bottom, the mesh was always finer for half the thickness 0.5*h*. d) Magnified view on contact between probe and sample. e) Boundary conditions applied at bottom of the sample.**

set to be frictionless and the normal behavior was set to be hard contact for pressure overclosure. To develop the model for force-displacement curves, the interfacial nodes at the contact between the probe and the sample were not tied together. To develop a model for pressure-displacement curves, the interfacial nodes were tied together. Mesh type was always C3D8H and reduced integration was employed. A sketch of the meshed model is shown in S-Figure 2 a, b, c. The mesh was finer close to the interfacial contact between the probe and the sample (S-Figure 2 b), and both the sample and the probe mesh were refined accordingly for different contact radii. For all sample thicknesses, $h$, the mesh was finer from the top to half the thickness, $0.5h$ (S-Figure 2 c). In all simulations, the mesh has been refined to the extent that the change of contact force by further refining the mesh was less than 1%.

Sketches of the boundary conditions applied are shown in S-Figure 2 d, e. For the sample, boundary conditions were defined such that displacement of the bottom surface of the sample was prevented in all three dimensions. Also, displacement in all three dimensions was prevented for one single edge at the bottom. Displacement of the remaining three bottom edges was prevented in both directions perpendicular to the direction of probe displacement.

### 3.2 *Development of Analytical Model for Pressure–Displacement Curves*

As shown in the main manuscript, the experimentally determined slope of a pressure-displacement curve, $(\partial(\Delta p)/\partial\delta)$, is constant and mainly affected by geometric constraints given by $a/h$ and $b/a$. An analytical model for $(\partial(\Delta p)/\partial\delta)$ was developed based on FEA simulations of volume–displacement curves having a slope of $(\partial(\Delta V)/\partial\delta)$. By assuming ideal gas behavior (S-eq. 1), $\Delta V$ can be approximated to be linearly proportional to $\Delta p$ (S-eq. 2 (S-Figure 3 d)).

$$\frac{\Delta p}{p_0} = \left( \frac{1}{\left(1 + \frac{\Delta V}{V}\right)} - 1 \right) \qquad \text{S-eq. 1}$$

$$\frac{\Delta p}{p_0} \approx - \frac{\Delta V}{V} \qquad \text{S-eq. 2}$$

$p_0$ is the initial pressure and $V$ is the volume of air enclosed by the annular contact. Using $(\partial(\Delta V)/\partial\delta)$ can be converted to $(\partial(\Delta p)/\partial\delta)$ via S-eq. 2.

$(\partial(\Delta V)/\partial\delta)$ curves for loading (indentation) and unloading (probe retraction) were simulated. To ensure interfacial contact between the probe and the sample during retraction, their interfacial surface nodes were tied together. The volume-change, $\Delta V$, for a given probe displacement, $\delta$, was calculated from the displacement of surface nodes of the sample inside the inner contact area. A custom-written

Matlab® code was employed to calculate $\Delta V$ manually from the displacement of the surface nodes, $u_z$, in the direction parallel to $\delta$.[I] $\Delta V$ corresponds to the volume of an imaginary, three-dimensional cell formed between $u_z$ of all surface nodes and $\delta$ (S-Figure 3 a, b)). Our Matlab® code uses the "convhull" function[2] to calculate the volume of the imaginary cells.[II] The slope of the volume–displacement curves, $(\partial(\Delta V)/\partial\delta)$, was found to be constant and almost identical for loading and unloading (S-Figure 3 c)). Consistent with the experimental results shown in in the main manuscript, simulated values of $\Delta V$ are

[I] While Abaqus® has functions that could principally be used to calculate the volume-change,[1] a straightforward implementation of these functions into the geometry of our model geometry is not trivial. Thus, we decided to calculate volume-change manually.

[II] To justify the use of the "convhull" function by Matlab®, we entered the coordinates of real elements in FEA our model into our code. The volume calculated by our code results in the same element volume, "EVOL" that is provided by Abaqus®.

independent of $E$.

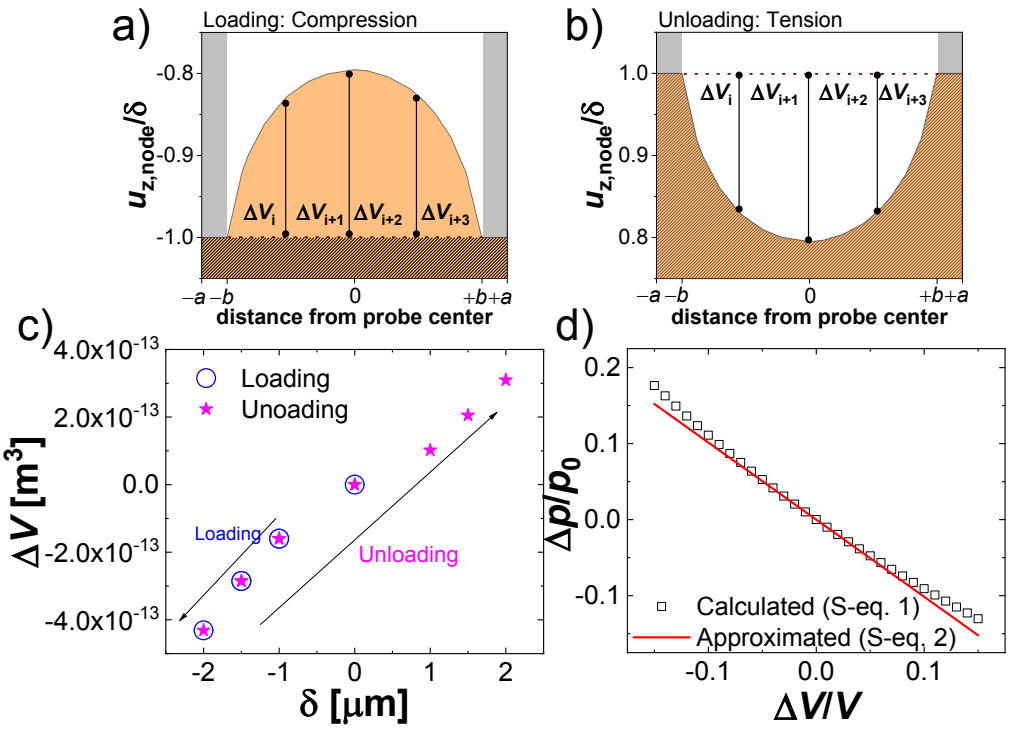


**S-Figure 3: Illustration of estimation of volume-change $\Delta V$ during loading (a) and unloading (b). $u_{z,node}$ are z-coordinates of element nodes and δ is the probe displacement. $\Delta V$ is the total of the volume changes $\Delta V_i$. $\Delta V_i$ was estimated for three-dimensional imaginary cells formed between nodes of surface elements of the sample and corresponding nodes with identical x- and y-coordinates but z-coordinates at $u_{z,node}/\delta = 1$. $\Delta V_i$ was calculated for three-dimensional models; two-dimensional sketches are shown for clarity. c) Exemplary simulated relationships between $\Delta V$ and δ between a rigid probe and an incompressible elastic sample (ν = 0.4999) d) Symbols: Relationship between volume- and pressure-change calculated according to the ideal gas law (S-eq. 1). Line: approximation according to S-eq. 2.**

# 4 Material Properties of Samples

## 4.1 *Experimental Determination of Compliance*

The compliance, $C$, was determined from the inverse slope of the initial linear part of the unloading portion of the force–displacement curve for each sample. This method has been used previously and has been shown to be a robust and reliable method to determine $C$.[3] An exemplary force–displacement curve is shown in S-Figure 4. S-Figure 4 a) shows the entire curve and shows S-Figure 4 c) magnified view on the initial part during unloading and compares the data with the linear fit. The slope was determined as follows: Starting from the first data points during unloading, the moving average from $i$ to $i + j$ for corresponding force, $F$, and displacement, $\delta$, data points was calculated. The slope, $K$, was calculated as:

$$K = \frac{F(2i + j) - F(i)}{\delta(2i + j) - \delta(i)} \qquad \text{S-eq. 3}$$

$j$ is the distance between neighboring data sets, and was always at least 20. Over the entire curve, $N$ values, of the slope $K$ were calculated. To determine the slope of the initial linear part during unloading, $K$ was plotted against $N$. $N = 1$ corresponds to the first value of the slope with respect to the start of the unloading portion of the curve. To determine the value of the slope that was used to calculate $C$, the average value of the slope, $K_{avg}$, from $K\,(N = 1)$ until $K\,(N_{max})$, with $N_{max}$ being the last value where $K$ can be approximated to be constant was taken (S-Figure 4 b). This method ensured a good fit of the initial force–displacement curve during unloading (S-Figure 4 c). If necessary, the window size, $j$, was increased to a larger value to ensure a better fit. $C$ corresponds to $1/K_{avg}$.

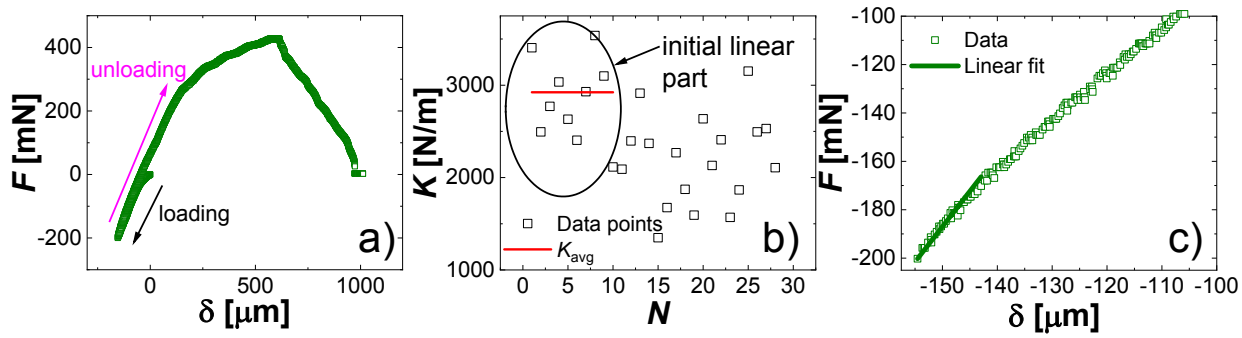


**S-Figure 4: a) Complete force-displacement curve, exemplary shown for VHB500. b) Values of slope *K* calculated along the force-displacement curve in the initial stages of unloading. The circle encloses the slopes for the initial linear part that were averaged to calculate $K_{avg}$. In this region, *K* is assumed to be constant. c) Comparison between data and linear fit in a magnified view on the initial part of unloading of the same force-displacement curve shown in panel a).**

Values of $C$ are given in S-Table 1 and S-Table 2 for $b/a = 0.79$ and $b/a = 0.71$, respectively. The standard deviation is very small proving that our method to determine $C$ is robust. Typically, the values were averaged over multiple runs and multiple samples for the same material.

**S-Table 1: Compliance of all samples for $b/a = 0.79$. Numbers in parentheses are the standard deviation. All PDMS samples have a thickness, $h$, of around ~2 mm unless stated otherwise.**

| **Sample** | ***a*/*h*** | ***C* [m/mN]** |
|---|---|---|
| PDMS30:1 | 0.7 (0.00) | 1.6 (0.02) |
| PDMS40:1 | 0.8 (0.02) | 2.6 (0.05) |
| PDMS50:1 ($h \sim 2$ mm) | 0.7 (0.01) | 5.8 (0.02) |
| PDMS50:1 ($h \sim 0.4$ mm) | 3.4 (0.03) | 2.5 (0.01) |
| PDMS60:1 | 0.7 (0.01) | 13.3 (0.45) |
| PEHAX | 6.5 (0.39) | 0.3 (0.00) |
| VHB500 | 2.7 (0.03) | 0.4 (0.00) |
| VHB1000 | 1.3 (0.03) | 0.6 (0.02) |

**S-Table 2: Compliance of all samples for $b/a = 0.71$. Numbers in parentheses are the standard deviation. All PDMS samples have a thickness, $h$, of around ~2 mm unless stated otherwise.**

| Sample | $a/h$ | $C$ [m/mN] |
|---|---|---|
| PDMS30:1 | 0.4 (0.00) | 2.2 (0.01) |
| PDMS40:1 | 0.5 (0.00) | 4.2 (0.15) |
| PDMS50:1 ($h \sim 2$ mm) | 0.4 (0.01) | 11.7 (0.56) |
| PDMS50:1 ($h \sim 0.4$ mm) | 1.8 (0.11) | 4.6 (0.23) |
| PDMS60:1 | 0.4 (0.02) | 24.7 (0.85) |
| PEHAX | 4.4 (0.02) | 0.7 (0.02) |
| VHB500 | 1.7 (0.02) | 0.6 (0.06) |
| VHB1000 | 0.9 (0.01) | 0.9 (0.05) |

## 4.2 *Values of Elastic Moduli*

The elastic moduli obtained by fitting the compliance values according to eqs. 1–3 in the main manuscript are given in S-Table 3. While the curing and processing history affect the modulus of the final PDMS network, the herein calculated values of the moduli of the PDMS samples are similar to literature values of PDMS samples with identical base:cross-linker ratio.[4]

**S-Table 3: Elastic moduli for all samples obtained by fitting experimentally determined values of the compliance. Numbers in parentheses are the standard deviation. All PDMS samples have a thickness, *h*, of around ~2 mm unless stated otherwise.**

| **Sample** | ***E* [kPa]** |
|---|---|
| PDMS30:1 | 113 (21) |
| PDMS40:1 | 62 (4) |
| PDMS50:1 ($h \sim 2$ mm) | 26 (2) |
| PDMS50:1 ($h \sim 0.4$ mm) | 24 (2) |
| PDMS60:1 | 11 (1) |
| PEHAX | 68 (14) |
| VHB500 | 191 (20) |
| VHB1000 | 214 (18) |

### 4.3 *Calculation of Energy Release Rates for Interfacial Detachment and Location of Samples on 3D Failure Map*

To confirm the validity of the location of each sample on the 2D-phase map in Figure 6 b), contact adhesion measurements between the sample and a hemisphere were conducted. We analyzed the force, displacement, and corresponding contact area during the contact adhesion tests to calculate the energy release rate, $G$, following the quasi-elastic analysis by Shull *et al*.[5] In all experiments, the probe displacement rate was 1 μm/s. The probe was a glass hemisphere with a radius of 2.6 mm. While the probes used for the annular-probe tack tests are made of steel, we used glass hemispheres for these measurements to allow the interfacial area to be visualized and measured. The critical energy release rate for interfacial failure, $G_c$, for the steel/sample interfaces may differ compared to those determined for glass/sample interfaces, but we anticipate that these differences will be less than uncertainty introduced by using adhesion measurements in the absence of interfacial area measurements.

To determine the value of $G_c$, $G$ was plotted as a function of measured contact radius. During the initial retraction of the probe, the contact radius remains at its maximum value, $a_{max}$, until a critical value of $G$ is obtained and the contact radius decreases. This value of $G$ was identified as $G_c$ and is denoted as $G_{c,sphere}$ in S-Table 4 and in the following discussion in order to remind the reader of the conditions for these measurements. Please find full details on the analysis procedure in Ref. 5.

**S-Table 4: Values of $G_{c,sphere}$ determined from contact adhesion tests using a glass hemisphere at a probe displacement rate of 1 μm/s for different samples.**

| Sample | $G_{c,sphere}$ [J/m$^2$] |
|---|---|
| PDMS30:1 | 0.06 (0.03) |
| PDMS40:1 | 0.08 (0.02) |
| PDMS50:1 ($h$ ~ 2000 μm) | 0.17 (0.06) |
| PDMS50:1 ($h$ ~ 400 μm) | 0.36 (0.09) |
| PDMS 60:1 | 0.12 (0.04) |
| PEHAX | 0.8 (0.1) |
| VHB500 | 1.2 (0.3) |
| VHB1000 | 1.5 (0.3) |

To estimate the location of each sample on the three-dimensional failure map shown in Figure 6 a), we calculated $G_{c,sphere}/(Ea)$ for each sample. $E$ is the elastic modulus of the sample, which was provided in S-Table 3, and $a$ is the outer radius of the annular-probe. The estimated values for $G_{c,sphere}/(Ea)$ were compared to the values of $G_c/Ea$ on the surface in Figure 6a at the corresponding a/h and b/a values. If $G_{c,sphere}/(Ea)$ is greater than $G_c/(Ea)$ from the surface map, then failure is anticipated to occur by cavitation within the annular interfacial area. If $G_{c,sphere}/(Ea)$ is less than $G_c/(Ea)$ on the surface map, then failure is anticipated to occur by edge crack propagation from either the inner or outer edge.

For all samples, $G_{c,sphere}/(Ea)$ is less than $G_c/(Ea)$ on the surface map. For all samples except for PEHAX, this is consistent with contact area images for these samples that indicated failure by edge crack propagation (see Figure 6 b, c). However, for PEHAX, contact images suggest failure by cavitation (see S-Video 1). Comparing the values of $G_{c,sphere}/(Ea)$ with $G_c/(Ea)$ for the surface map in Figure 6 a, the values are both similar, and $G_{c,sphere}/(Ea)$ is only slightly below $G_c/(Ea)$. We attribute this divergence to

using different materials as probes in the sphere- and annular-probe tack tests. Accordingly, we do not include PEHAX in the 2D failure map presented in Figure 6 b).

**S-Table 5: Comparison of $G_c/(Ea)$ for the glass sphere ($G_{c,sphere}$) and the upper limit for edge crack failure for the annular probe ($G_c$). Note, that the annular probe was made of steel and the glass probe was made of glass.**

| Sample | Annular probe, $a$ = 1.36 mm, $b/a$ = 0.79 | | | Annular probe, $a$ = 0.8 mm, $b/a$ = 0.71 | | |
|---|---|---|---|---|---|---|
| | $a/h$ | $G_{c,sphere}/(Ea)$ | $G_c/(Ea)$ from surface map in Figure 6 a) | $a/h$ | $G_{c,sphere}/(Ea)$ | $G_c/(Ea)$ from surface map in Figure 6 a) |
| PDMS30:1 | 0.7 (0.00) | $3.9\ 10^{-4}$ | $5.8\ 10^{-2}$ | 0.4 (0.00) | $6.6\ 10^{-4}$ | $9.3\ 10^{-2}$ |
| PDMS40:1 | 0.8 (0.02) | 9.5 10−4 | $5.8\ 10^{-2}$ | 0.5 (0.00) | $1.6\ 10^{-3}$ | $9.3\ 10^{-2}$ |
| PDMS50:1 ($h \sim 2000$ μm) | 0.7 (0.01) | $4.9\ 10^{-3}$ | $5.9\ 10^{-2}$ | 0.4 (0.01) | $8.3\ 10^{-3}$ | $9.4\ 10^{-2}$ |
| PDMS50:1 ($h \sim 400$ μm) | 3.4 (0.03) | $1.1\ 10^{-2}$ | $3.9\ 10^{-2}$ | 1.8 (0.11) | $1.8\ 10^{-2}$ | $9.4\ 10^{-2}$ |
| PDMS 60:1 | 0.7 (0.01) | $7.8\ 10^{-3}$ | $5.9\ 10^{-2}$ | 0.4 (0.02) | $1.3\ 10^{-2}$ | $4.1\ 10^{-2}$ |
| PEHAX | 6.5 (0.39) | $1.2\ 10^{-2}$ | $2.9\ 10^{-2}$ | 4.4 (0.02) | $2.0\ 10^{-2}$ | $7.0\ 10^{-2}$ |
| VHB500 | 2.7 (0.03) | $4.7\ 10^{-3}$ | $4.7\ 10^{-2}$ | 1.7 (0.02) | $7.9\ 10^{-3}$ | $8.4\ 10^{-2}$ |
| VHB1000 | 1.3 (0.03) | $5.2\ 10^{-3}$ | $5.5\ 10^{-2}$ | 0.9 (0.01) | $8.8\ 10^{-3}$ | $5.7\ 10^{-2}$ |

## 4.4 *Absolute Values of Peak Force and Debonding Energy for Open and Closed Contact*

Absolute values of the peak force, $F_{max}$, and the debonding energy, $w_{deb}$, as calculated according to eq. 17 in the main manuscript, for open and closed annular contact are given in S-Table 6.

**S-Table 6: Values of $F_{max}$ and $w_{deb}$ for open and closed annular contact ($b/a$ = 0.79). Numbers in parentheses are the standard deviation.**

| Sample | $F_{max}$ (open) [mN] | $F_{max}$ (closed) [mN] | $w_{deb}$ (open) [J/m$^2$] | $w_{deb}$ (closed) [J/m$^2$] |
|---|---|---|---|---|
| PDMS30:1 | 34 (2) | 14 (7) | 0.6 (0.1) | 0.5 (0.1) |
| PDMS40:1 | 38 (2) | 47 (3) | 1.3 (0.1) | 1.8 (0.2) |
| PDMS50:1 | 22 (4) | 34 (1) | 1.1 (0.3) | 2.1 (0.2) |
| PDMS60:1 | 15 (2) | 23 (2) | 2.8 (0.9) | 5.3 (1.0) |
| PEHAX | 353 (9) | 507 (18) | 102.4 (6.7) | 117.6 (14.6) |
| VHB500 | 483 (27) | 733 (50) | 102.8 (27.7) | 230.7 (38.5) |
| VHB1000 | 408 (18) | 514 (24) | 164.3 (12.9) | 227.8 (41.8) |

# 5 References


1. Abaqus MIT Documentation, *About surface-based fluid cavities*, link: https://abaqus-docs.mit.edu/2017/English/SIMACAEANLRefMap/simaanl-c-surfacebasedcavityover.htm, last visited on March 08, 2021.
2. Matlab® documentation for "convhull" function: https://www.mathworks.com/help/matlab/ref/convhull.html, last visited on March 08, 2021.
3. M. D. Bartlett, A. B. Croll, D. R. King, B. M. Paret, D. J. Irschick, A. J. Crosby, *Adv. Mater.* **2012**, *24*, 1078–1083.
4. J. D. Glover, C. E. McLaughlin, M. K. McFarland, J. T. Pham, *J. Polym. Sci.* **2020**, *58*, 343–351.
5. A. J. Crosby, K. R. Shull, *J. Polym. Sci. B Polym. Phys.* **1999**, *37*, 3455–3472.